

# Spectral-Geometric Neural Fields for Pose-Free LiDAR View Synthesis

Yinuo Jiang Jun Cheng Yiran Wang<sup>\*†</sup> Cheng Cheng<sup>\*</sup>  
 School of AIA, Huazhong University of Science and Technology  
 {jiangyinuo, chengjun, wangyiran, c\_cheng}@hust.edu.cn

## Abstract

Neural Radiance Fields (NeRF) have shown remarkable success in image novel view synthesis (NVS), inspiring extensions to LiDAR NVS. However, most methods heavily rely on accurate camera poses for scene reconstruction. The sparsity and textureless nature of LiDAR data also present distinct challenges, leading to geometric holes and discontinuous surfaces. To address these issues, we propose SG-NLF, a pose-free LiDAR NeRF framework that integrates spectral information with geometric consistency. Specifically, we design a hybrid representation based on spectral priors to reconstruct smooth geometry. For pose optimization, we construct a confidence-aware graph based on feature compatibility to achieve global alignment. In addition, an adversarial learning strategy is introduced to enforce cross-frame consistency, thereby enhancing reconstruction quality. Comprehensive experiments demonstrate the effectiveness of our framework, especially in challenging low-frequency scenarios. Compared to previous state-of-the-art methods, SG-NLF improves reconstruction quality and pose accuracy by over 35.8% and 68.8%. Our work can provide a novel perspective for LiDAR view synthesis.

## 1. Introduction

Novel View Synthesis (NVS) is a vital task for 3D perception, with broad applications in scene understanding [22, 23, 42, 44], autonomous driving [45, 48], and robotics [12, 37]. The goal of NVS is to generate novel views from one or more given source views [25]. While most existing works focus on synthesizing camera views, LiDAR sensors play an important role in autonomous systems for accurate perception. Extending NVS to LiDAR (*i.e.*, LiDAR NVS) can significantly broaden perceptual field [52, 55] and enhance robustness of autonomous driving systems [21, 41, 43].

Despite remarkable progress in image-based NVS, LiDAR NVS presents distinct challenges due to the inherent

<sup>\*</sup> Corresponding author.

<sup>†</sup> Project leader.

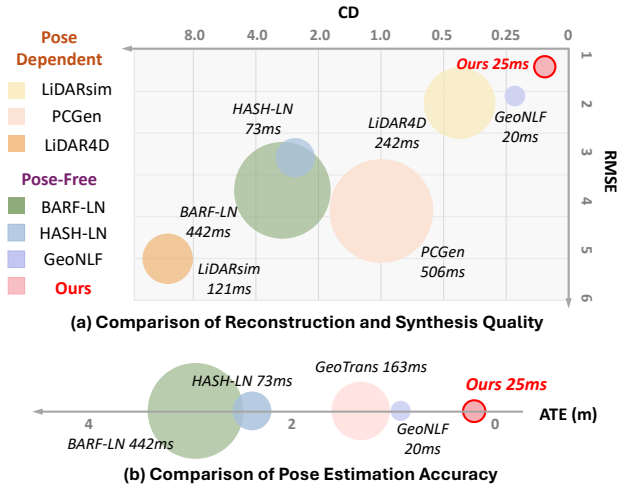


Figure 1. (a) **Reconstruction and synthesis quality.** The X-axis shows Chamfer Distance (CD) for point cloud reconstruction on the low-frequency KITTI-360 dataset [26, 50]. The Y-axis shows RMSE for range depth and intensity synthesis. Circle area represents inference time. Lower CD and RMSE mean better reconstruction and synthesis. Our framework outperforms prior work by large margins. (b) **Pose accuracy.** The axis represents Absolute Trajectory Error (ATE) for pose estimation. Our SG-NLF demonstrates higher accuracy compared to existing NeRF-based models.

sparsity of LiDAR point clouds and their lack of texture information [14–16, 24]. Traditional LiDAR simulation approaches [6, 18, 38] reconstruct explicit surfaces from aggregated point clouds and perform physically-based ray casting to render novel LiDAR views. However, such simulation methods struggle to accurately model the intensity or ray-drop characteristics of actual LiDAR points [11, 52].

Neural Radiance Fields (NeRF) [32] provide a promising alternative by implicitly reconstructing scenes in continuous representation space through volume rendering. Recent advances have successfully extended NeRF to LiDAR novel view synthesis [11, 39, 50–53, 55], demonstrating superior performance over traditional methods [6, 18, 38]. However, existing methods still face two critical challenges. First, as shown in Fig. 1, prior arts [11, 39, 51–53, 55] rely on

accurate camera poses, which are often impractical to obtain [10]. Recent pose-free methods like GeoNLF [50] attempt to resolve this by simultaneous multi-view registration and neural reconstruction. However, the dependence on pairwise alignments makes it difficult to ensure global pose accuracy. Second, both pose-dependent and pose-free frameworks [11, 39, 50, 52, 55] typically employ geometric interpolation (*e.g.*, multi-resolution hash encoding [33]) for neural field rendering. Due to the sparsity and irregularity of LiDAR data, such interpolated features often struggle to reconstruct continuous surfaces, leading to geometric inconsistency in textureless regions (shown in Fig. 2). These challenges are further exacerbated in low-frequency LiDAR sequences, where large inter-frame motion and reduced overlap undermine multi-view consistency [50, 52].

To address the aforementioned challenges, we propose **SG-NLF**, a spectral-geometric neural LiDAR fields framework for novel view synthesis and pose estimation. Specifically, we design a hybrid representation that integrates spectral embeddings with geometric encoding to reconstruct smooth and consistent geometry. For pose optimization, we construct a confidence-aware graph and establish geometric constraints through feature compatibility, achieving global pose estimation. We further introduce an adversarial learning strategy that enforces cross-frame consistency and reconstruction quality through discriminative supervision. As shown in Fig. 1, our SG-NLF can simultaneously achieve high-quality LiDAR view synthesis and accurate pose estimation, outperforming previous state-of-the-art methods.

We evaluate our SG-NLF on the KITTI-360 [26] and nuScenes [4] datasets, focusing on low-frequency sequences that span hundreds of meters [50]. Compared to the leading method GeoNLF [50], SG-NLF reduces Chamfer Distance by **35.8%** and Absolute Trajectory Error by **68.8%** on nuScenes, with consistently significant improvements across all metrics. Additionally, on standard-frequency sequences with complex scenes [39], SG-NLF continues to outperform prior arts, demonstrating the generalization. Our contributions are summarized as follows:

- We propose SG-NLF, a novel framework that integrates spectral-geometric information for simultaneous high-quality view synthesis and accurate pose estimation.
- We design a hybrid representation that combines spectral embeddings for geometry-consistent reconstruction and a confidence-aware graph for global pose optimization.
- Comprehensive experiments prove our state-of-the-art performance even in challenging low-frequency scenes.

## 2. Related Work

**LiDAR Simulation.** Traditional LiDAR simulators [6, 18] generate point clouds through physics-based ray casting in virtual environments, showing a significant domain gap

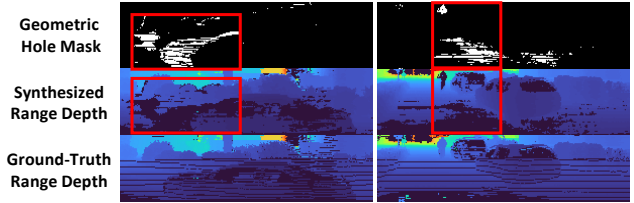


Figure 2. **Geometric Inconsistency** [11, 39, 50]. The geometric hole mask is generated by comparing rendered opacity with ground truth LiDAR measurements. White regions in rectangular boxes (first row) highlight areas where these methods fail to reconstruct geometry. Comparisons between second and third rows further show these holes lead to poor-quality synthesized views.

compared to real-world data [52, 55]. Reconstruct-then-simulate approaches [20, 31] attempt to bridge this gap by combing realistic LiDAR data. LiDARsim [31] performs reconstruction using mesh surfel representation, while PC-Gen [20] reconstructs directly from point clouds and employs rasterization for rendering. However, these methods still rely on explicit surface reconstruction, making them difficult to accurately model the intensity or ray drop characteristics of actual LiDAR points [39, 50, 52, 55].

**NeRF for LiDAR View Synthesis.** Neural Radiance Fields (NeRF) [32] have shown remarkable progress in image novel view synthesis [11, 25], with many variants built on voxel grids [9, 29] and multi-resolution hash encodings [33]. Recent studies have extended NeRF to LiDAR novel view synthesis, demonstrating performance that surpasses traditional simulation approaches [20, 31]. Early methods such as NeRF-LiDAR [53] leverage both RGB images and LiDAR point clouds for scene reconstruction. However, such multi-modal data are not always available in practical applications [52]. LiDAR-NeRF [39] and NFL [11] first introduce differentiable frameworks for LiDAR NVS, which synthesize depth, intensity, and ray-drop probability without relying on RGB inputs. Subsequent works like LiDAR4D [55] and STGC [52] further extend the framework to dynamic scenes by incorporating temporal priors. A commonality across these methods is the sole reliance on geometric interpolation for neural field rendering. Due to the inherent sparsity and irregularity of LiDAR data, such representation often struggles to reconstruct continuous surfaces, leading to geometric inconsistency in textureless regions. To overcome this limitation, we propose a novel hybrid representation that combines spectral embeddings to reconstruct smooth and consistent geometry.

**Pose-free NeRF.** In addition to the reconstruction challenges, most existing LiDAR NVS methods [11, 39, 52, 53, 55] exhibit a strong dependence on known accurate poses for rendering, which are often difficult to acquire in real-world scenarios [27]. Inspired by the image-based pose-free methods like BARF [27] and HASH [10], GeoNLF [50] introduces pose-free neural LiDAR fields to optimize multi-

view registration and neural reconstruction simultaneously. Despite this progress, the pairwise alignment constraints limit the global trajectory accuracy. In this paper, we propose a confidence-aware pose graph based on spectral-geometric feature compatibility for global optimization.

### 3. Methodology

We propose SG-NLF, a spectral-geometric neural LiDAR fields framework for pose-free view synthesis. In this section, we first introduce the problem formulation and preliminary for LiDAR NeRF with pose optimization, followed by a detailed description of our proposed SG-NLF method.

#### 3.1. Overview

**Problem Formulation.** Given LiDAR point cloud sequences  $\{\mathcal{S}_i\}_{i=0}^N$  captured in a large-scale outdoor scene, our goal is to recover their global poses  $\{\mathbf{T}_i\}_{i=0}^N$  and jointly reconstruct the scene as a continuous implicit representation. The reconstructed representation can synthesize realistic LiDAR point clouds from an arbitrary new viewpoint.

**Preliminary for NeRF with Pose Optimization.** Following prior LiDAR NeRF frameworks [39, 50, 52, 55], we project LiDAR point clouds into range images, where each laser beam is modeled as a ray  $\mathbf{r}(t) = \mathbf{o} + t\mathbf{d}$  originating from the sensor center  $\mathbf{o}$  with direction  $\mathbf{d}$ . The neural function is queried at 3D points sampled along  $\mathbf{r}$  to predict their depth value  $z$  and volume density  $\sigma$ . Volume rendering is employed to compute the pixel depth  $\hat{D}(\mathbf{r})$ :

$$\hat{D}(\mathbf{r}) = \sum_{i=1}^N T_i \left(1 - e^{-\sigma_i \delta_i}\right) z_i, T_i = \exp\left(-\sum_{j=1}^{i-1} \sigma_j \delta_j\right), \quad (1)$$

where  $\delta$  is the distance between samples and  $T$  represents the accumulated transmittance. Intensity and ray-drop probability are predicted separately in the same way [39, 50].

While original NeRFs require precise camera poses for rendering, pose-free methods treat them as learnable parameters [27, 50]. We follow prior work [28, 50] to optimize poses in their corresponding Lie algebra space. Each pose is parameterized by a 6D vector  $\boldsymbol{\xi} = [\boldsymbol{\rho}, \boldsymbol{\phi}]^\top \in \mathbb{R}^6$  and updated by computing a small increment  $\Delta\boldsymbol{\xi}$  in the algebra space, such that  $\boldsymbol{\xi}' = \boldsymbol{\xi} + \Delta\boldsymbol{\xi}$ . The transformation is recovered from the vector  $\boldsymbol{\xi}$  via the exponential mapping:

$$\mathbf{T} = \exp(\boldsymbol{\xi}^\wedge) = \sum_{n=0}^{\infty} \frac{1}{n!} (\boldsymbol{\xi}^\wedge)^n = \begin{bmatrix} \mathbf{R} & \mathbf{J}\boldsymbol{\rho} \\ \mathbf{0}^\top & 1 \end{bmatrix}, \quad (2)$$

where  $\mathbf{R} = \exp(\boldsymbol{\phi}^\wedge)$  and  $\mathbf{J} = \sum_{n=0}^{\infty} \frac{1}{(n+1)!} (\boldsymbol{\phi}^\wedge)^n$ . The Jacobian  $\mathbf{J}$  couples rotation and translation components in the Lie algebra update, which may lead to non-intuitive optimization trajectories when using momentum-based optimizers. We follow prior arts [28, 50] to omit the Jacobian  $\mathbf{J}$  from the translation term for more stable convergence.

**Overview of SG-NLF Framework.** Fig. 3 illustrates an overview of the proposed SG-NLF framework. Existing methods [11, 39] rely solely on interpolating 3D positions to extract features and render neural fields, which often results in geometric inconsistency. In contrast, our SG-NLF introduces a hybrid representation that integrates discrete geometric encodings with continuous spectral embeddings, enabling more effective and robust reconstruction. Regarding pose optimization, compared to previous pose-free approaches with pairwise alignment constraints [50], SG-NLF constructs a confidence-aware graph based on hybrid feature compatibility, achieving global pose optimization. The optimized poses, together with the hybrid features, are fed into NeRF to synthesize LiDAR views  $\hat{\mathcal{S}}$ . To further improve cross-frame consistency, SG-NLF employs a discriminative supervision mechanism that distinguishes between the real depth maps (obtained from the ground truth point clouds  $\mathcal{S}_{ij}$  that are transformed into the cross-frame coordinate system) and the fake depth maps (generated from synthesized and transformed point clouds  $\hat{\mathcal{S}}_{ij}$ ).

#### 3.2. Hybrid Spectral-Geometric Representation

Our representation builds upon multi-resolution hash grid encoding [33] to extract geometric features  $\mathbf{f}_{\text{geo}}(\mathbf{x})$ , capturing local structures and high-frequency details [11, 55]. However, the inherent sparsity of LiDAR point clouds means that interpolation-based features alone are insufficient, as they struggle to reconstruct complete and coherent surfaces in unobserved regions due to the lack of global structural priors [13]. To overcome this limitation, we augment the geometric representation with spectral embeddings, which exhibit intrinsic isometry invariance and are aware of the underlying surface geometry [1, 13, 19].

While spectral embeddings are traditionally obtained via an inefficient and non-differentiable offline eigen-decomposition of the Laplace-Beltrami operator (LBO) [19, 36], we draw inspiration from recent neural spectral approaches [1, 13], which optimize a set of MLPs and approximate the first  $K$  LBO eigenfunctions in a differentiable manner to obtain spectral embeddings. We construct the underlying scene geometry following SNS [1] and represent the scalar fields using MLPs. The spectral embeddings are then defined as  $\mathbf{f}_{\text{spe}}(\mathbf{x}) = [\Psi_0(\mathbf{x}), \Psi_1(\mathbf{x}), \dots, \Psi_K(\mathbf{x})]^\top$ , where  $\Psi_0(\mathbf{x})$  is the constant eigenfunction corresponding to the zero eigenvalue. To ensure our learned embeddings exhibit the intrinsic spectral properties, we optimize for the first  $K$  non-constant eigenfunctions by minimizing the Rayleigh quotient. Our implementation of the Laplace-Beltrami operator follows the mean curvature formulation [1]. To ensure uniform sampling on the implicit surface, we adopt the rejection sampling strategy from SNS [1] and sample  $M$  points  $\{\hat{\mathbf{x}}_i\}_{i=1}^M$  from the surface, where  $M$  is the number of Monte Carlo samples used for discrete ap-

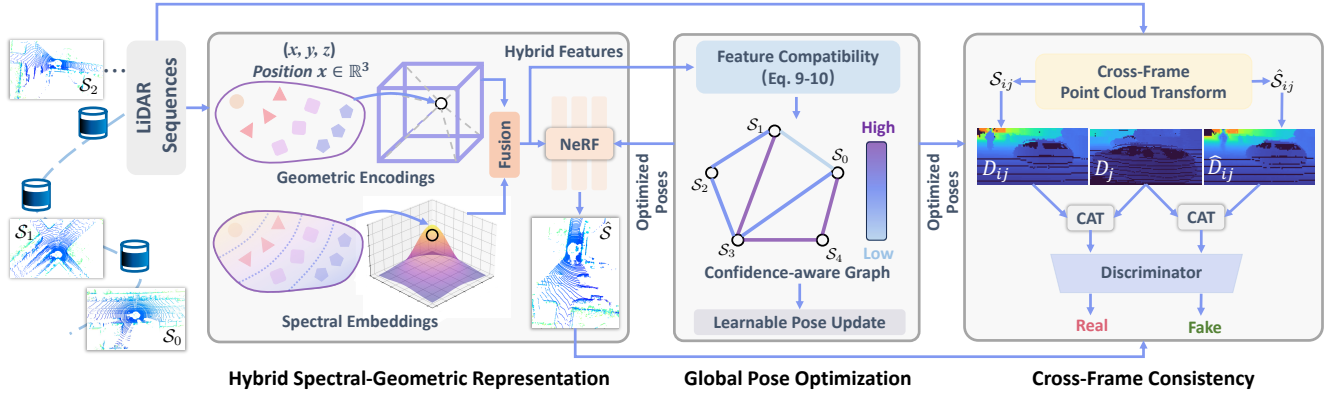


Figure 3. **Overview of the SG-NLF.** Given multi-view LiDAR sequences  $\{\mathcal{S}_i\}_{i=0}^N$ , SG-NLF employs a hybrid representation that combines discrete geometric encoding with continuous spectral embedding for effective reconstruction. The hybrid features are utilized to construct a confidence-aware graph for global pose optimization. The optimized poses and hybrid features are fed into NeRF to synthesize novel views  $\hat{\mathcal{S}}$ . To further enhance cross-frame consistency, SG-NLF distinguishes between the real depth maps (obtained from ground truth point clouds  $\mathcal{S}_{ij}$  that are transformed into cross-frame coordinates) and fake depth maps (obtained from synthesized and transformed  $\hat{\mathcal{S}}_{ij}$ ).

proximation. For each sampled point  $\hat{\mathbf{x}}_i$ , we compute the local area element  $dA_i$  using the First Fundamental Form:

$$dA_i = \sqrt{E_i \cdot G_i - F_i^2}, \quad (3)$$

where  $E_i = \|\mathbf{t}_{i,1}\|^2$ ,  $G_i = \|\mathbf{t}_{i,2}\|^2$ , and  $F_i = \langle \mathbf{t}_{i,1}, \mathbf{t}_{i,2} \rangle$  are coefficients of the First Fundamental Form, with  $\mathbf{t}_{i,1}$  and  $\mathbf{t}_{i,2}$  being tangent plane basis vectors computed via automatic differentiation of the implicit surface mapping [1]. The surface gradient of the eigenfunction is computed by projecting its 3D spatial gradient onto the tangent plane:

$$\nabla_{\Sigma} \Psi(\hat{\mathbf{x}}_i) = \nabla \Psi(\hat{\mathbf{x}}_i) - \langle \nabla \Psi(\hat{\mathbf{x}}_i), \mathbf{n}(\hat{\mathbf{x}}_i) \rangle \mathbf{n}(\hat{\mathbf{x}}_i), \quad (4)$$

where  $\mathbf{n}(\hat{\mathbf{x}}_i)$  denotes the unit normal vector, computed as the normalized cross product of tangent plane basis vectors:  $\mathbf{n}(\hat{\mathbf{x}}_i) = \frac{\mathbf{t}_{i,1} \times \mathbf{t}_{i,2}}{\|\mathbf{t}_{i,1} \times \mathbf{t}_{i,2}\|}$ . Using these robust geometric definitions, the discrete Rayleigh quotient [1] is formulated as:

$$\mathcal{R}_{\Sigma}(\Psi_i) = \frac{\sum_{j=1}^M \|\nabla_{\Sigma} \Psi_i(\hat{\mathbf{x}}_j)\|^2 dA_j}{\sum_{j=1}^M \Psi_i^2(\hat{\mathbf{x}}_j) dA_j}. \quad (5)$$

To ensure that the learned eigenfunctions form a valid orthonormal basis on the surface, we impose both orthogonality and normalization constraints [1]. The orthogonality loss enforces distinct spectral components:

$$\mathcal{L}_{\text{ortho}} = \sum_{i=1}^K \sum_{\substack{m=1 \\ m \neq i}}^K \left( \sum_{j=1}^M \Psi_i(\hat{\mathbf{x}}_j) \Psi_m(\hat{\mathbf{x}}_j) dA_j \right)^2, \quad (6)$$

while the normalization loss maintains unit  $L^2$ -norm for each eigenfunction:

$$\mathcal{L}_{\text{norm}} = \sum_{i=1}^K \left( \sum_{j=1}^M \Psi_i^2(\hat{\mathbf{x}}_j) dA_j - 1 \right)^2. \quad (7)$$

The overall spectral loss is formulated as:

$$\mathcal{L}_{\text{spe}} = \sum_{i=1}^K \mathcal{R}_{\Sigma}(\Psi_i) + \lambda_n \mathcal{L}_{\text{norm}} + \lambda_o \mathcal{L}_{\text{ortho}}, \quad (8)$$

where  $\lambda_n$  and  $\lambda_o$  are balancing coefficients. The geometric encodings and spectral embeddings are progressively fused during training to form a hybrid representation  $\mathbf{f}_{\text{hyb}}(\mathbf{x})$ , which is subsequently used by the rendering network to predict depth, intensity, and ray-drop probability.

### 3.3. Global Pose Optimization

We introduce a pose graph that is dynamically constructed through spectral-geometric feature matching. The graph is defined as  $\mathcal{G} = (\mathcal{V}, \mathcal{E})$ . Each vertex  $v_i \in \mathcal{V}$  represents a LiDAR point cloud  $\mathcal{S}_i$  with its global pose  $\mathbf{T}_i$ , while edge  $(i, j) \in \mathcal{E}$  represents constraints between  $\mathcal{S}_i$  and  $\mathcal{S}_j$ . Compared to approaches [50] that rely solely on enforcing constraints between temporal neighbors, our edge set  $\mathcal{E}$  incorporates both sequential edges and non-adjacent edges with high feature compatibility, thereby jointly enforcing inter-frame alignment and global trajectory accuracy.

To identify reliable non-adjacent edges, we first leverage our fused spectral-geometric features  $\mathbf{f}_{\text{hyb}}(\mathbf{x})$  to establish point-wise correspondences. For the  $m$ -th point in  $\mathcal{S}_i$ , denoted as  $\mathbf{x}_m^i$ , its corresponding feature is defined as  $\mathbf{f}_m^i = \mathbf{f}_{\text{hyb}}(\mathbf{x}_m^i)$ . Similarly, for the  $n$ -th point in  $\mathcal{S}_j$ , the feature is  $\mathbf{f}_n^j = \mathbf{f}_{\text{hyb}}(\mathbf{x}_n^j)$ . We adopt a coarse-to-fine Mutual Nearest Neighbor (MNN) strategy to build reliable correspondences. For a candidate scan pair  $(\mathcal{S}_i, \mathcal{S}_j)$ , the coarse correspondence set is constructed as:

$$\mathcal{M}_c^{ij} = \left\{ (m, n) \mid \begin{aligned} \|\mathbf{f}_m^i - \mathbf{f}_n^j\|_2 &= \min_{n'} \|\mathbf{f}_m^i - \mathbf{f}_{n'}^j\|_2 \wedge \\ \|\mathbf{f}_n^j - \mathbf{f}_m^i\|_2 &= \min_{m'} \|\mathbf{f}_n^j - \mathbf{f}_{m'}^i\|_2 \end{aligned} \right\}, \quad (9)$$

where  $\wedge$  denotes the logical AND operator. Then, a refined correspondence set  $\mathcal{M}_f^{ij}$  is generated by reapplying MNN matching in  $\mathcal{M}_c^{ij}$ . We calculate the mean cosine similarity of feature pairs in  $\mathcal{M}_f^{ij}$  as the edge compatibility score:

$$E^{ij} = \frac{1}{|\mathcal{M}_f^{ij}|} \sum_{(m,n) \in \mathcal{M}_f^{ij}} \frac{\mathbf{f}_m^i \cdot \mathbf{f}_n^j}{\|\mathbf{f}_m^i\|_2 \|\mathbf{f}_n^j\|_2}, \quad (10)$$

which serves as the basis for edge inclusion. An edge  $(i, j)$  is added to  $\mathcal{E}$  if  $E^{ij}$  exceeds an adaptive threshold and threshold is progressively increased during training to enforce stricter edge selection. To further mitigate the influence of inaccurate edges, each edge is weighted by the correspondence spatial consistency. For  $(i, j) \in \mathcal{E}$ , we follow prior arts [2, 35] to compute the spatial consistency score  $P_{mn}$  for point correspondence  $(m, n) \in \mathcal{M}_f^{ij}$ :

$$P_{mn} = \frac{1}{N_m} \sum_{\substack{(m',n') \in \mathcal{M}_f^{ij}, \\ m \neq m'}} \mathbb{I}(|d_{mm'}^i - d_{nn'}^j| < \tau_d), \quad (11)$$

where  $N_m$  is the count of correspondence pairs in  $\mathcal{M}_f^{ij}$  excluding  $(m, n)$ .  $d_{mm'}^i = \|\mathbf{x}_m^i - \mathbf{x}_{m'}^i\|_2$  and  $d_{nn'}^j = \|\mathbf{x}_n^j - \mathbf{x}_{n'}^j\|_2$  represent the length distances between correspondence pairs.  $\tau_d$  is a distance preservation threshold. We compute the edge weight for each edge based on the average spatial consistency:

$$\alpha^{ij} = \frac{1}{|\mathcal{M}_f^{ij}|} \sum_{(m,n) \in \mathcal{M}_f^{ij}} P_{mn}. \quad (12)$$

The pose graph loss is formulated as the weighted Chamfer Distance loss:

$$\mathcal{L}_{\text{graph}} = \sum_{(i,j) \in \mathcal{E}} \alpha^{ij} \cdot \mathcal{L}_{\text{cd}}^{ij}, \quad (13)$$

where  $\mathcal{L}_{\text{cd}}^{ij}$  is Chamfer Distance [8] computed following prior arts [50]. Refer to supplement for more formulations.

### 3.4. Cross-frame Consistency

Most existing LiDAR NeRF frameworks [39, 50, 55] only rely on pixel-wise supervision of range images, which penalizes photometric errors within individual frames but overlooks structural information. To enhance cross-frame consistency, we introduce an adversarial learning strategy that evaluate quality of reconstructed geometry and accuracy of pose estimation through discriminative supervision.

For temporally adjacent frames  $(i, j)$ , we compute the estimated relative pose as  $\hat{\mathbf{T}}_{ij} = \hat{\mathbf{T}}_j^{-1} \hat{\mathbf{T}}_i$ . This transformation is applied to the reconstructed point cloud  $\hat{\mathcal{S}}_i$ , yielding the transformed point cloud  $\hat{\mathcal{S}}_{ij}$  in the coordinate system of frame  $j$ . We then render a depth map  $\hat{D}_{ij}$  from

$\hat{\mathcal{S}}_{ij}$  and concatenate  $\hat{D}_{ij}$  with the ground truth depth map  $D_j$  of frame  $j$ , forming  $\mathbf{I}_{\text{fake}} = [\hat{D}_{ij}, D_j]$ . Correspondingly, the ground truth point cloud  $\mathcal{S}_i$  is transformed using the ground truth relative pose  $\mathbf{T}_{ij}$  and projected to produce  $D_{ij}$ . This is concatenated with  $D_j$  to construct the real sample  $\mathbf{I}_{\text{real}} = [D_{ij}, D_j]$ . By incorporating paired depth maps from adjacent frames, the discriminator is able to assess not only the quality of per-frame reconstructions but also the cross-frame geometric alignment [49].

Our discriminator follows a multi-scale PatchGAN design [7], capable of detecting geometric misalignments at both global and local levels. During discriminator training, we utilize a hinge loss formula to improve stability:

$$\mathcal{L}_{\text{con}} = \max(0, 1 - \Phi(\mathbf{I}_{\text{real}})) + \max(0, 1 + \Phi(\mathbf{I}_{\text{fake}})), \quad (14)$$

where  $\Phi$  represents the discriminator network. When training the NeRF generator, the consistency loss is defined as  $\mathcal{L}_{\text{con}} = -\Phi(\mathbf{I}_{\text{fake}})$ . In addition to the discriminative supervision, we also follow prior arts [39, 50, 55] to incorporate 2D range image supervision. The overall training objective for neural LiDAR fields combines the consistency loss, range image loss, and spectral loss. Please refer to the supplement for more details on optimization strategies.

## 4. Experiment

In this section, we first describe experimental setup for evaluation. Following this, we compare SG-NLF with previous LiDAR view synthesis methods [20, 39, 50, 55] to demonstrate our state-of-the-art performance. Furthermore, we conduct ablation studies to expound on our specific designs.

### 4.1. Experimental Setup

**Datasets.** We conduct experiments on two autonomous driving datasets: KITTI-360 [26] and nuScenes [4]. KITTI-360 [26] is equipped with a LiDAR of 64-beam, a 26.4° vertical FOV, and an acquisition frequency of 10 Hz. NuScenes [4] is captured by a 32-beam LiDAR with a 40° vertical FOV and an acquisition frequency of 20 Hz.

**Experimental Settings.** To evaluate the reconstruction performance in low-frequency sequences, we follow GeoNLF [50] to resample both datasets at 2 Hz. For KITTI-360 [26], we extract 24 frames from resampled sequences, retaining one sample every eight frames for testing. For nuScenes [4], we extract 36 frames and retain one sample every nine frames for testing. In addition, we conduct experiments in standard-frequency scenarios following LiDAR-NeRF [39], extracting 64 consecutive frames and four equidistant test samples from KITTI-360 [26]. LiDAR poses are perturbed with additive noise using a standard deviation of 20° in rotation and 3m in translation [50].

**Evaluation Metrics.** We evaluate the reconstruction accuracy of LiDAR point clouds using the Chamfer Distance

Table 1. **Comparisons with state-of-the-art methods on KITTI-360 [26] dataset with a low-frequency setting [50].** We compare our method with pose-dependent [20, 31, 55] and pose-free methods [10, 27, 35, 50]. For approaches not originally designed for LiDAR NVS [10, 27, 35], we follow GeoNLF [50] and adopt LiDAR-NeRF [39] for reconstruction. For pose-dependent methods, we employ ground-truth poses for synthesis. We color the best results as red and the second-best as orange.

| Method               | Point Cloud |          | Depth   |        |        |        |         | Intensity |        |        |        |         |
|----------------------|-------------|----------|---------|--------|--------|--------|---------|-----------|--------|--------|--------|---------|
|                      | CD↓         | F-score↑ | RMSE↓   | MedAE↓ | LPIPS↓ | SSIM↑  | PSNR↑   | RMSE↓     | MedAE↓ | LPIPS↓ | SSIM↑  | PSNR↑   |
| LiDARsim [31]        | 11.0426     | 0.5975   | 10.1994 | 1.3881 | 0.5588 | 0.3888 | 17.9423 | 0.2089    | 0.1254 | 0.6463 | 0.0824 | 13.6127 |
| PCGen [20]           | 1.0356      | 0.7862   | 7.5672  | 0.7066 | 0.5333 | 0.3744 | 20.6219 | 0.2139    | 0.1063 | 0.5930 | 0.1070 | 13.4243 |
| BARF-LN [27, 39]     | 3.1001      | 0.6156   | 7.5767  | 2.0583 | 0.5779 | 0.2834 | 22.5759 | 0.2121    | 0.1575 | 0.7121 | 0.1468 | 11.9778 |
| HASH-LN [10, 39]     | 2.6913      | 0.6082   | 6.3005  | 2.1686 | 0.5176 | 0.3752 | 22.6196 | 0.2404    | 0.1502 | 0.6508 | 0.1602 | 12.9286 |
| GeoTrans-LN [35, 39] | 0.5753      | 0.8116   | 4.4291  | 0.2023 | 0.3896 | 0.5330 | 25.6137 | 0.2709    | 0.1589 | 0.5578 | 0.2578 | 12.9707 |
| LiDAR4D [55]         | 0.2760      | 0.8843   | 4.7303  | 0.0785 | 0.3368 | 0.6197 | 24.7282 | 0.1459    | 0.0524 | 0.3883 | 0.3406 | 16.9512 |
| GeoNLF [50]          | 0.2363      | 0.9178   | 4.0293  | 0.1009 | 0.3900 | 0.6272 | 25.2758 | 0.1495    | 0.1525 | 0.5379 | 0.3165 | 16.5813 |
| SG-NLF(Ours)         | 0.1695      | 0.9191   | 2.9514  | 0.0544 | 0.0701 | 0.9270 | 28.7068 | 0.1089    | 0.0368 | 0.2026 | 0.5751 | 19.2652 |

Table 2. **Comparisons with state-of-the-art methods on nuScenes [4] dataset with a low-frequency setting [50].** We color the best results as red and the second-best as orange. The notations are consistent with the KITTI-360 [26] dataset in Table 1 above.

| Method               | Point Cloud |          | Depth   |        |        |        |         | Intensity |        |        |        |         |
|----------------------|-------------|----------|---------|--------|--------|--------|---------|-----------|--------|--------|--------|---------|
|                      | CD↓         | F-score↑ | RMSE↓   | MedAE↓ | LPIPS↓ | SSIM↑  | PSNR↑   | RMSE↓     | MedAE↓ | LPIPS↓ | SSIM↑  | PSNR↑   |
| LiDARsim [31]        | 16.7623     | 0.4308   | 12.3483 | 1.9971 | 0.3125 | 0.3889 | 16.2553 | 0.0858    | 0.0355 | 0.1713 | 0.2897 | 21.3989 |
| PCGen [20]           | 2.2608      | 0.6139   | 12.6586 | 0.7055 | 0.2365 | 0.4389 | 12.6586 | 0.0865    | 0.0235 | 0.1530 | 0.3707 | 21.3643 |
| BARF-LN [27, 39]     | 1.2695      | 0.7589   | 8.2414  | 0.1123 | 0.1432 | 0.6856 | 20.8900 | 0.3920    | 0.0144 | 0.1023 | 0.6119 | 26.2330 |
| HASH-LN [10, 39]     | 0.9691      | 0.8011   | 7.8353  | 0.0441 | 0.1190 | 0.6543 | 20.6244 | 0.0459    | 0.0135 | 0.0954 | 0.6279 | 26.8870 |
| GeoTrans-LN [35, 39] | 4.1587      | 0.2993   | 10.7899 | 2.1529 | 0.1445 | 0.3671 | 17.5885 | 0.0679    | 0.0256 | 0.1149 | 0.3476 | 23.6211 |
| LiDAR4D [55]         | 0.5668      | 0.7444   | 11.1964 | 0.0847 | 0.0685 | 0.5983 | 17.0920 | 0.0599    | 0.0180 | 0.0639 | 0.5401 | 24.4753 |
| GeoNLF [50]          | 0.2408      | 0.8647   | 5.8208  | 0.0281 | 0.0727 | 0.7746 | 22.9472 | 0.0378    | 0.0100 | 0.0774 | 0.7368 | 28.6078 |
| SG-NLF(Ours)         | 0.1545      | 0.9097   | 3.0706  | 0.0278 | 0.0191 | 0.9398 | 28.4094 | 0.0299    | 0.0078 | 0.0349 | 0.8679 | 30.4987 |

(CD) and the F-score value (error threshold of 5cm) [39, 50, 52, 55]. For novel view synthesis, we report depth and intensity errors of the projected range images using Root Mean Square Error (RMSE) and Median Absolute Error (MedAE), while overall variance is measured with LPIPS [54], SSIM [46], and PSNR. For pose evaluation, we follow GeoNLF [50] to use standard odometry metrics, including Absolute Trajectory Error (ATE) and Relative Pose Error ( $RPE_r$  for rotation and  $RPE_t$  for translation).

**Implementation Details.** Consistent with prior arts [39, 50, 52, 55], the entire point cloud scene is scaled within the unit cube space and 768 points are uniformly sampled along each laser beam. Our SG-NLF is implemented on PyTorch [34] and optimized with the Adam [17] optimizer. Each scene is trained for 60k iterations with a batch size of 4,096 rays. The initial learning rate is 0.01 and follows a linear power decay schedule, as in previous work [50]. We construct hash grids based on tiny-cuda-nn. All experiments are conducted on a single GeForce NVIDIA RTX 4090 GPU. Refer to the supplement for more details.

## 4.2. Comparisons in LiDAR View Synthesis

**Comparisons in Low-frequency Scenarios.** We compare our method with state-of-the-art approaches for LiDAR novel view synthesis, including pose-dependent [20, 31, 55] and pose-free methods [10, 27, 35, 50]. For approaches not originally designed for LiDAR NVS [10, 27, 35], we follow GeoNLF [50] and adopt LiDAR-NeRF [39] for reconstruction. For pose-dependent methods, we employ ground-truth

poses for synthesis. For pose-free approaches, we follow prior arts [47, 50] to obtain test view poses for rendering.

Table 1 demonstrates our state-of-the-art performance on KITTI-360 [26] with a low-frequency setting [50]. Our SG-NLF significantly surpasses all these methods in point cloud reconstruction and range image synthesis. Compared to the second-best pose-free method GeoNLF [50], SG-NLF reduces CD by 28.3%, while improving depth PSNR and intensity PSNR by 13.6% and 16.2% respectively. Notably, even when LiDAR4D [55] utilizes ground-truth poses for reconstruction and synthesis, pose-free SG-NLF still outperforms it by over 38.5%, 37.5%, and 25.4% for CD, depth RMSE, and intensity RMSE, showing the efficacy of proposed architectures in challenging low-frequency scenarios.

Similarly, in Table 2, compared to the leading method [50], SG-NLF reduces reconstruction errors by over 37.5%, 47.2%, 73.7%, 20.9%, and 54.9% for CD, depth RMSE, depth LPIPS, intensity RMSE, and intensity LPIPS on low-frequency nuScenes [4, 50]. This superior performance demonstrates the effectiveness of our spectral-geometric design for sparse LiDAR data.

**Comparisons in Standard-frequency Scenarios.** Following prior arts [39, 55], we evaluate SG-NLF on the standard-frequency KITTI-360 dataset [26]. As shown in Table 3, compared to state-of-the-art pose-dependent methods [11, 20, 31, 39, 55], our pose-free SG-NLF still achieves more accurate reconstruction and synthesis. While the pose-free GeoNLF [50] underperforms pose-dependent LiDAR4D [55] on most metrics, SG-NLF improves depth

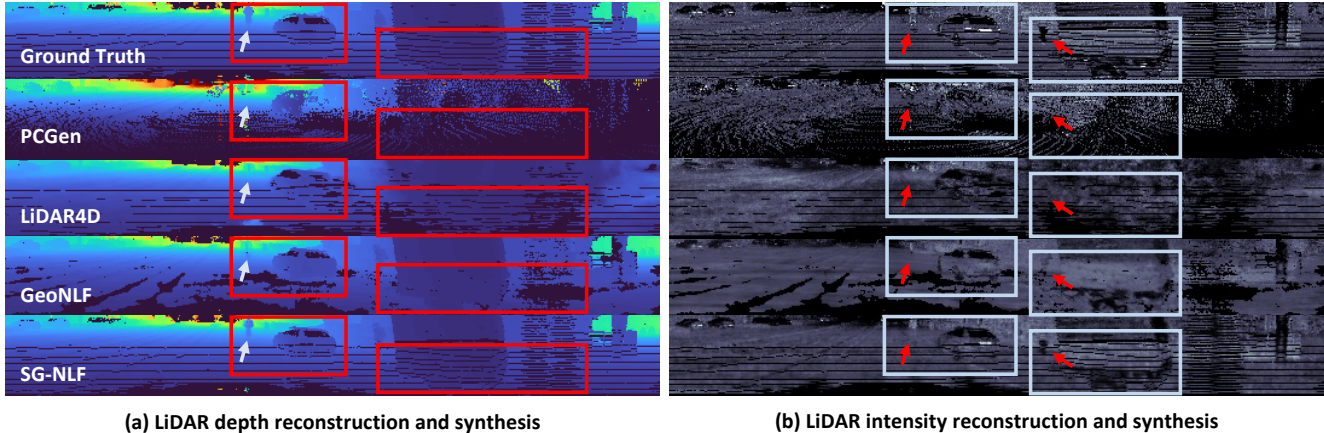


Figure 4. **Qualitative comparisons for LiDAR range depth and intensity reconstruction.** Both pose-dependent [20, 55] and pose-free methods [50] are compared. Regions with obvious differences are highlighted in the rectangular boxes and arrows.

Table 3. **Comparisons on the KITTI-360 [26] dataset with standard-frequency setting [39].** We compare SG-NLF with state-of-the-art pose-dependent methods [11, 20, 31, 39, 55] and pose-free model [50]. We color the best results as red and the second-best as orange.

| Method          | Point Cloud |          | Depth  |        |        |        |         | Intensity |        |        |        |         |
|-----------------|-------------|----------|--------|--------|--------|--------|---------|-----------|--------|--------|--------|---------|
|                 | CD↓         | F-score↑ | RMSE↓  | MedAE↓ | LPIPS↓ | SSIM↑  | PSNR↑   | RMSE↓     | MedAE↓ | LPIPS↓ | SSIM↑  | PSNR↑   |
| LiDARsim [31]   | 2.2249      | 0.8667   | 6.5470 | 0.0759 | 0.2289 | 0.7157 | 21.7746 | 0.1532    | 0.0506 | 0.2502 | 0.4479 | 16.3045 |
| PCGen [20]      | 0.2090      | 0.8597   | 4.8838 | 0.1785 | 0.5210 | 0.5062 | 24.3050 | 0.2005    | 0.0818 | 0.6100 | 0.1248 | 13.9606 |
| NKSR [11]       | 0.5780      | 0.8685   | 4.6647 | 0.0698 | 0.2295 | 0.7052 | 22.5390 | 0.1565    | 0.0536 | 0.2429 | 0.4200 | 16.1159 |
| LiDAR-NeRF [39] | 0.0923      | 0.9226   | 3.6801 | 0.0667 | 0.3523 | 0.6043 | 26.7663 | 0.1557    | 0.0549 | 0.4212 | 0.2768 | 16.1683 |
| LiDAR4D [55]    | 0.0894      | 0.9264   | 3.2370 | 0.0507 | 0.1313 | 0.7218 | 27.8840 | 0.1343    | 0.0404 | 0.2127 | 0.4698 | 17.4529 |
| GeoNLF [50]     | 0.1855      | 0.9157   | 2.7144 | 0.0589 | 0.2495 | 0.7797 | 29.3912 | 0.1484    | 0.0613 | 0.3483 | 0.3617 | 16.5709 |
| SG-NLF (Ours)   | 0.0867      | 0.9322   | 1.8519 | 0.0515 | 0.0864 | 0.9168 | 32.7245 | 0.1054    | 0.0380 | 0.1802 | 0.6122 | 19.5468 |

PSNR and intensity PSNR by over 17.4% and 11.9% compared to LiDAR4D. This demonstrates the generalization of our framework in complex real-world scenes. The aforementioned results showcase our effectiveness in both low-frequency and standard-frequency scenarios.

**Qualitative Comparisons.** Fig. 4 visualizes depth and intensity reconstruction results in challenging low-frequency scenarios from KITTI-360 [26]. We compare our method with both pose-dependent [20, 55] and pose-free [50] models. As highlighted by the rectangles and arrows, LiDAR4D [55] and GeoNLF [50] produce blurry results with missing structural details. In contrast, our SG-NLF generates accurate depth and intensity maps that depict smooth and complete structures while preserving clear boundaries (e.g., pedestrians and vehicles). Furthermore, the black horizontal lines in these maps represent the predicted raydrop mask. While competing methods [20, 50, 55] exhibit substantial erroneous predictions, our results align closely with the ground truth. These improvements can be attributed to our effective spectral-geometric hybrid representation and cross-frame consistency strategy. Please refer to the supplement for more quantitative and visual experimental results.

### 4.3. Comparisons in Pose Estimation

**Quantitative Comparisons.** We follow prior art [50] to compare SG-NLF with both pairwise registration base-

lines [3, 5, 30, 35, 40] and pose-free NeRF methods [10, 27, 39, 50]. For pairwise methods, we perform registration between adjacent frames in an odometry-like manner. All estimated trajectories are aligned with the ground truth using a Sim(3) transform of known scale [50]. As shown in Table 4, SG-NLF outperforms both pairwise registration and pose-free NeRF approaches on the KITTI-360 [26, 50] and nuScenes [4, 50] datasets. Specifically, SG-NLF reduces ATE by over 56.4% and 68.8% on KITTI-360 and nuScenes compared to the second-best GeoNLF [50].

**Qualitative Comparisons.** To visually evaluate pose accuracy, we transform point cloud sequences into a unified scene using estimated global poses. We color-code the composite scene by height (a spectrum from yellow to purple) in Fig. 5. Accurate poses produce coherent color gradations (see ground truth), while pose errors result in misalignment and color fragmentation (see input sequences). BARF-LN [27, 39] retains significant noise in road areas, indicating inaccurate estimation. Conversely, our SG-NLF produces accurately aligned and geometrically consistent point clouds, achieving quality closest to the ground truth.

### 4.4. Ablation Studies

**Hybrid Representation Analysis.** We presents an ablation study of our spectral embeddings with comparisons to GeoNLF [50] in Table 5. While GeoNLF relies on geo-

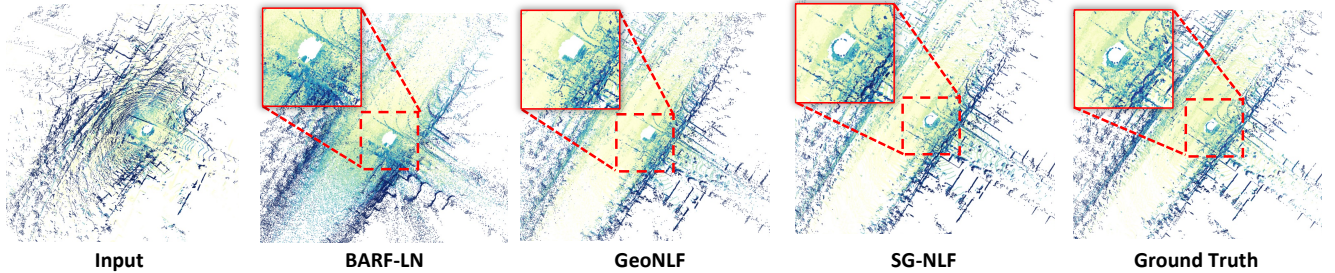


Figure 5. **Visual comparisons for pose estimation.** We transform input sequences into a unified scene using estimated global poses and color-code the composite scene by height. We compare with pose-free methods [27, 39, 50]. Best view zoomed in on-screen for details.

Table 4. **Pose estimation comparisons on KITTI-360 [26, 50] and nuScenes [4, 50].** We compare with registration baselines [3, 5, 30, 35, 40] and pose-free NeRF methods [10, 27, 39, 50].

| Method           | KITTI-360 |                         |                        | nuScenes |                         |                        |
|------------------|-----------|-------------------------|------------------------|----------|-------------------------|------------------------|
|                  | ATE (m)↓  | RPE <sub>r</sub> (deg)↓ | RPE <sub>t</sub> (cm)↓ | ATE (m)↓ | RPE <sub>r</sub> (deg)↓ | RPE <sub>t</sub> (cm)↓ |
| ICP [3]          | 1.894     | 1.019                   | 30.383                 | 1.131    | 0.647                   | 15.410                 |
| MICP [5]         | 1.483     | 1.419                   | 35.584                 | 2.519    | 1.101                   | 38.840                 |
| HRegNet [30]     | 7.423     | 9.083                   | 290.160                | 7.815    | 2.173                   | 120.913                |
| SGHR [40]        | 2.539     | 0.906                   | 95.576                 | 9.557    | 0.699                   | 30.383                 |
| BARF-LN [27, 39] | 2.763     | 2.203                   | 199.740                | 5.244    | 0.819                   | 210.331                |
| HASH-LN [10, 39] | 2.666     | 2.171                   | 196.791                | 4.151    | 0.832                   | 180.282                |
| GeoTrans [35]    | 0.246     | 0.213                   | 6.081                  | 0.892    | 0.363                   | 16.097                 |
| GeoNLF [50]      | 0.170     | 0.205                   | 5.449                  | 0.228    | 0.103                   | 7.058                  |
| SG-NLF(Ours)     | 0.074     | 0.127                   | 2.003                  | 0.071    | 0.158                   | 4.096                  |

Table 5. **Hybrid Representation Analysis.** Ablation study of geometric encodings (GE) and spectral embeddings (SE) on nuScenes [4], with comparisons to GeoNLF [50].

| Method         | GE | SE | Point Cloud CD↓ | Depth PSNR↑ | Intensity PSNR↑ |
|----------------|----|----|-----------------|-------------|-----------------|
| GeoNLF [50]    | ✓  | ✗  | 0.241           | 22.947      | 28.608          |
| SG-NLF(w/o GE) | ✗  | ✓  | 0.181           | 26.853      | 29.032          |
| SG-NLF(Ours)   | ✓  | ✓  | 0.155           | 28.409      | 30.499          |

metric interpolation for rendering, our SG-NLF (*w/o* GE) reconstructs more smooth and complete geometry through spectral embeddings (shown in Fig. 6). However, it tends to miss several high-frequency details. The hybrid representation can achieve high-quality reconstruction both quantitatively and qualitatively by integrating low-frequency spectral embeddings with high-frequency geometric encodings.

**Efficacy of SG-NLF Components.** In Table 6, we ablate on our three core components: hybrid spectral-geometric representation (HR), global pose optimization (GP), and cross-frame consistency (CFC). We adopt the same baseline as GeoNLF [50], *i.e.*, a geometric encoding model without pose estimation. For the ablation of hybrid spectral-geometric representation, we retain only geometric encodings for feature extraction, resulting in decreased pose accuracy and reconstruction quality. Comparing the first and third rows, even without pose optimization, incorporating cross-frame consistency supervision effectively regular-

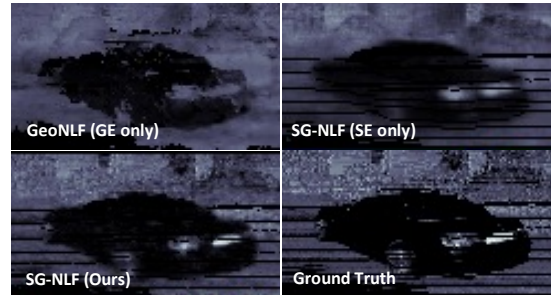


Figure 6. **Qualitative comparison for hybrid representation.**

Table 6. **Efficacy of SG-NLF Components.** Ablation on the hybrid spectral-geometric representation (HR), global pose optimization (GP), and cross-frame consistency (CFC) using nuScenes dataset [4]. We adopt the same baseline as GeoNLF [50].

| Method         | HR | GP | CFC | Point Cloud CD↓ | Depth PSNR↑ | Intensity PSNR↑ | Pose ATE(m)↓ |
|----------------|----|----|-----|-----------------|-------------|-----------------|--------------|
| Baseline       | ✗  | ✗  | ✗   | 0.618           | 21.321      | 25.856          | 1.328        |
| <i>w/o</i> HR  | ✗  | ✓  | ✓   | 0.217           | 25.103      | 28.425          | 0.204        |
| <i>w/o</i> GP  | ✓  | ✗  | ✓   | 0.463           | 23.942      | 27.549          | 0.798        |
| <i>w/o</i> CFC | ✓  | ✓  | ✗   | 0.182           | 26.597      | 29.303          | 0.076        |
| Ours           | ✓  | ✓  | ✓   | 0.155           | 28.409      | 30.499          | 0.071        |

izes training and mitigates performance degradation. Conversely, as shown in the fourth row, removing CFC leads to cross-frame inconsistency and performance degradation.

## 5. Conclusion

In this paper, we propose SG-NLF, a spectral-geometric neural fields for pose-free LiDAR view synthesis. Different from previous methods that rely on geometric interpolation, our approach introduces a hybrid representation that integrates spectral embeddings to reconstruct smooth and continuous geometry. We also design a confidence-aware graph optimizer for robust global pose estimation and an adversarial learning strategy to enforce cross-frame consistency. Comprehensive experiments demonstrate the effectiveness of the proposed SG-NLF framework. Our work can provide a novel perspective on the accurate LiDAR view synthesis.

**Limitations.** We currently provide one effective implementation of the SG-NLF. In future work, more techniques can be explored for different application scenarios.

## References

- [1] Neural Geometry Processing via Spherical Neural Surfaces, author=Williamson, Romy and Mitra, Niloy J. In *Computer Graphics Forum*, page e70021. Wiley Online Library, 2025. 3, 4
- [2] Xuyang Bai, Zixin Luo, Lei Zhou, Hongkai Chen, Lei Li, Zeyu Hu, Hongbo Fu, and Chiew-Lan Tai. PointDSC: Robust point cloud registration using deep spatial consistency. In *Proceedings of the IEEE/CVF Conference on Computer Vision and Pattern Recognition*, pages 15859–15869, 2021. 5
- [3] Paul J Besl and Neil D McKay. Method for registration of 3-d shapes. In *Sensor fusion IV: control paradigms and data structures*, pages 586–606. Spie, 1992. 7, 8
- [4] Holger Caesar, Varun Bankiti, Alex H Lang, Sourabh Vora, Venice Erin Liong, Qiang Xu, Anush Krishnan, Yu Pan, Giancarlo Baldan, and Oscar Beijbom. nuscenes: A multi-modal dataset for autonomous driving. In *Proceedings of the IEEE/CVF Conference on Computer Vision and Pattern Recognition*, pages 11621–11631, 2020. 2, 5, 6, 7, 8
- [5] Sungjoon Choi, Qian-Yi Zhou, and Vladlen Koltun. Robust reconstruction of indoor scenes. In *Proceedings of the IEEE Conference on Computer Vision and Pattern Recognition*, pages 5556–5565, 2015. 7, 8
- [6] Alexey Dosovitskiy, German Ros, Felipe Codevilla, Antonio Lopez, and Vladlen Koltun. CARLA: An open urban driving simulator. In *Conference on robot learning*, pages 1–16. PMLR, 2017. 1, 2
- [7] Patrick Esser, Robin Rombach, and Bjorn Ommer. Taming transformers for high-resolution image synthesis. In *Proceedings of the IEEE/CVF Conference on Computer Vision and Pattern Recognition*, pages 12873–12883, 2021. 5
- [8] Haoqiang Fan, Hao Su, and Leonidas J Guibas. A point set generation network for 3d object reconstruction from a single image. In *Proceedings of the IEEE conference on computer vision and pattern recognition*, pages 605–613, 2017. 5
- [9] Sara Fridovich-Keil, Alex Yu, Matthew Tancik, Qinhong Chen, Benjamin Recht, and Angjoo Kanazawa. Plenoxels: Radiance fields without neural networks. In *Proceedings of the IEEE/CVF Conference on Computer Vision and Pattern Recognition*, pages 5501–5510, 2022. 2
- [10] Hwan Heo, Taekyung Kim, Jiyoung Lee, Jaewon Lee, Soohyun Kim, Hyunwoo J Kim, and Jin-Hwa Kim. Robust camera pose refinement for multi-resolution hash encoding. In *International Conference on Machine Learning*, pages 13000–13016. PMLR, 2023. 2, 6, 7, 8
- [11] Shengyu Huang, Zan Gojcic, Zian Wang, Francis Williams, Yoni Kasten, Sanja Fidler, Konrad Schindler, and Or Litany. Neural lidar fields for novel view synthesis. In *Proceedings of the IEEE/CVF International Conference on Computer Vision*, pages 18236–18246, 2023. 1, 2, 3, 6, 7
- [12] Muhammad Zubair Irshad, Mauro Comi, Yen-Chen Lin, Nick Heppert, Abhinav Valada, Rares Ambrus, Zsolt Kira, and Jonathan Tremblay. Neural fields in robotics: A survey. *arXiv preprint arXiv:2410.20220*, 2024. 1
- [13] Puhua Jiang, Mingze Sun, and Ruqi Huang. Neural intrinsic embedding for non-rigid point cloud matching. In *Proceedings of the IEEE/CVF Conference on Computer Vision and Pattern Recognition*, pages 21835–21845, 2023. 3
- [14] YINUO JIANG, XIUCHUAN TANG, CHENG CHENG, and YE YUAN. A robust inlier identification algorithm for point cloud registration via  $\ell_0$ -minimization. *Advances in Neural Information Processing Systems*, 37:63124–63153, 2024. 1
- [15] YINUO JIANG, BEITONG ZHOU, XIAOYU LIU, QINGYI LI, and CHENG CHENG. GTINet: Global topology-aware interactions for unsupervised point cloud registration. *IEEE Transactions on Circuits and Systems for Video Technology*, 34(7):6363–6375, 2024.
- [16] YINUO JIANG, QINGYI LI, BINGHENG ZHANG, WANGJUN CHEN, JUN CHENG, and CHENG CHENG. Registration of Non-uniform LiDAR Scans with Large Pose Variations for Aircraft Assembly. *IEEE Transactions on Instrumentation and Measurement*, 2025. 1
- [17] Diederik P Kingma. Adam: A method for stochastic optimization. *arXiv preprint arXiv:1412.6980*, 2014. 6
- [18] Nathan Koenig and Andrew Howard. Design and use paradigms for gazebo, an open-source multi-robot simulator. In *2004 IEEE/RSJ international conference on intelligent robots and systems (IROS)(IEEE Cat. No. 04CH37566)*, pages 2149–2154. Ieee, 2004. 1, 2
- [19] Bruno Lévy and Hao Zhang. Spectral Mesh Processing. In *ACM SIGGRAPH 2010 Courses*, pages 1–312. 2010. 3
- [20] Chenqi Li, Yuan Ren, and Bingbing Liu. PCGen: Point cloud generator for lidar simulation. *arXiv preprint arXiv:2210.08738*, 2022. 2, 5, 6, 7
- [21] Jiaqi Li, Yiran Wang, Zihao Huang, Jinghong Zheng, Ke Xian, Zhiguo Cao, and Jianming Zhang. Diffusion-augmented depth prediction with sparse annotations. In *Proceedings of the 31st ACM International Conference on Multimedia*, pages 2865–2876, 2023. 1
- [22] Jiaqi Li, Yiran Wang, Jinghong Zheng, Zihao Huang, Ke Xian, Zhiguo Cao, and Jianming Zhang. Self-distilled depth refinement with noisy poisson fusion. *Advances in Neural Information Processing Systems*, 37:69999–70025, 2024. 1
- [23] Jiaqi Li, Yiran Wang, Jinghong Zheng, Junrui Zhang, Liao Shen, Tianqi Liu, and Zhiguo Cao. Ch3depth: Efficient and flexible depth foundation model with flow matching. In *Proceedings of the Computer Vision and Pattern Recognition Conference*, pages 7222–7232, 2025. 1
- [24] Qingyi Li, YINUO JIANG, JUN CHENG, WANGJUN CHEN, PENGYUAN ZHAO, XUECHUN QIAO, CHENG CHENG, and YE YUAN. AeroMamba: An Efficient Mamba-Based Approach for Large-Scale Point Cloud Registration in Aircraft Assembly. In *2025 IEEE/ASME International Conference on Advanced Intelligent Mechatronics (AIM)*, pages 1–8. IEEE, 2025. 1
- [25] Xingyi Li, Chaoyi Hong, Yiran Wang, Zhiguo Cao, Ke Xian, and Guosheng Lin. Symmnerf: Learning to explore symmetry prior for single-view view synthesis. In *Proceedings of the Asian conference on computer vision*, pages 1726–1742, 2022. 1, 2
- [26] Yiyi Liao, Jun Xie, and Andreas Geiger. Kitti-360: A novel dataset and benchmarks for urban scene understanding in 2d and 3d. *IEEE Transactions on Pattern Analysis and Machine Intelligence*, 45(3):3292–3310, 2022. 1, 2, 5, 6, 7, 8

- [27] Chen-Hsuan Lin, Wei-Chiu Ma, Antonio Torralba, and Simon Lucey. Barf: Bundle-adjusting neural radiance fields. In *Proceedings of the IEEE/CVF international conference on computer vision*, pages 5741–5751, 2021. 2, 3, 6, 7, 8
- [28] Yunzhi Lin, Thomas Müller, Jonathan Tremblay, Bowen Wen, Stephen Tyree, Alex Evans, Patricio A Vela, and Stan Birchfield. Parallel inversion of neural radiance fields for robust pose estimation. *arXiv preprint arXiv:2210.10108*, 2022. 3
- [29] Lingjie Liu, Jiatao Gu, Kyaw Zaw Lin, Tat-Seng Chua, and Christian Theobalt. Neural Sparse Voxel Fields. *Advances in Neural Information Processing Systems*, 33:15651–15663, 2020. 2
- [30] Fan Lu, Guang Chen, Yinlong Liu, Lijun Zhang, Sanqing Qu, Shu Liu, and Rongqi Gu. Hregnet: A hierarchical network for large-scale outdoor lidar point cloud registration. In *Proceedings of the IEEE/CVF International Conference on Computer Vision*, pages 16014–16023, 2021. 7, 8
- [31] Sivabalan Manivasagam, Shenlong Wang, Kelvin Wong, Wenyuan Zeng, Mikita Sazanovich, Shuhan Tan, Bin Yang, Wei-Chiu Ma, and Raquel Urtasun. Lidarsim: Realistic lidar simulation by leveraging the real world. In *Proceedings of the IEEE/CVF Conference on Computer Vision and Pattern Recognition*, pages 11167–11176, 2020. 2, 6, 7
- [32] Ben Mildenhall, Pratul P Srinivasan, Matthew Tancik, Jonathan T Barron, Ravi Ramamoorthi, and Ren Ng. Nerf: Representing scenes as neural radiance fields for view synthesis. *Communications of the ACM*, 65(1):99–106, 2021. 1, 2
- [33] Thomas Müller, Alex Evans, Christoph Schied, and Alexander Keller. Instant neural graphics primitives with a multiresolution hash encoding. *ACM transactions on graphics (TOG)*, 41(4):1–15, 2022. 2, 3
- [34] Adam Paszke, Sam Gross, Francisco Massa, Adam Lerer, James Bradbury, Gregory Chanan, Trevor Killeen, Zeming Lin, Natalia Gimelshein, Luca Antiga, et al. Pytorch: An imperative style, high-performance deep learning library. *Advances in Neural Information Processing Systems*, 32, 2019. 6
- [35] Zheng Qin, Hao Yu, Changjian Wang, Yulan Guo, Yuxing Peng, and Kai Xu. Geometric transformer for fast and robust point cloud registration. In *Proceedings of the IEEE/CVF Conference on Computer Vision and Pattern Recognition*, pages 11143–11152, 2022. 5, 6, 7, 8
- [36] Martin Reuter. Hierarchical shape segmentation and registration via topological features of laplace-beltrami eigenfunctions. *International Journal of Computer Vision*, 89(2): 287–308, 2010. 3
- [37] Amanjot S Sethi, William J Peine, Yousef Mohammadi, and Chandru P Sundaram. Validation of a novel virtual reality robotic simulator. *Journal of endourology*, 23(3):503–508, 2009. 1
- [38] Shital Shah, Debadeepta Dey, Chris Lovett, and Ashish Kapoor. Airlsim: High-fidelity visual and physical simulation for autonomous vehicles. In *Field and service robotics: Results of the 11th international conference*, pages 621–635. Springer, 2017. 1
- [39] Tang Tao, Longfei Gao, Guangrun Wang, Yixing Lao, Peng Chen, Hengshuang Zhao, Dayang Hao, Xiaodan Liang, Mathieu Salzmann, and Kaicheng Yu. Lidar-nerf: Novel lidar view synthesis via neural radiance fields. In *Proceedings of the 32nd ACM International Conference on Multimedia*, pages 390–398, 2024. 1, 2, 3, 5, 6, 7, 8
- [40] Haiping Wang, Yuan Liu, Zhen Dong, Yulan Guo, Yu-Shen Liu, Wenping Wang, and Bisheng Yang. Robust multiview point cloud registration with reliable pose graph initialization and history reweighting. In *Proceedings of the IEEE/CVF Conference on Computer Vision and Pattern Recognition*, pages 9506–9515, 2023. 7, 8
- [41] Yiran Wang, Xingyi Li, Min Shi, Ke Xian, and Zhiguo Cao. Knowledge distillation for fast and accurate monocular depth estimation on mobile devices. In *Proceedings of the IEEE/CVF Conference on Computer Vision and Pattern Recognition*, pages 2457–2465, 2021. 1
- [42] Yiran Wang, Zhiyu Pan, Xingyi Li, Zhiguo Cao, Ke Xian, and Jianming Zhang. Less is more: Consistent video depth estimation with masked frames modeling. In *Proceedings of the 30th ACM International Conference on Multimedia*, pages 6347–6358, 2022. 1
- [43] Yiran Wang, Min Shi, Jiaqi Li, Zihao Huang, Zhiguo Cao, Jianming Zhang, Ke Xian, and Guosheng Lin. Neural Video Depth Stabilizer. In *Proceedings of the IEEE/CVF International Conference on Computer Vision*, pages 9466–9476, 2023. 1
- [44] Yiran Wang, Min Shi, Jiaqi Li, Chaoyi Hong, Zihao Huang, Juewen Peng, Zhiguo Cao, Jianming Zhang, Ke Xian, and Guosheng Lin. Nvds<sup>+</sup>: Towards efficient and versatile neural stabilizer for video depth estimation. *IEEE transactions on pattern analysis and machine intelligence*, pages 1–18, 2024. 1
- [45] Yiran Wang, Jiaqi Li, Chaoyi Hong, Ruibo Li, Liusheng Sun, Xiao Song, Zhe Wang, Zhiguo Cao, and Guosheng Lin. TacoDepth: Towards Efficient Radar-Camera Depth Estimation with One-stage Fusion. In *Proceedings of the Computer Vision and Pattern Recognition Conference*, pages 10523–10533, 2025. 1
- [46] Zhou Wang, Alan C Bovik, Hamid R Sheikh, and Eero P Simoncelli. Image quality assessment: from error visibility to structural similarity. *IEEE Transactions on Image Processing*, 13(4):600–612, 2004. 6
- [47] Zirui Wang, Shangzhe Wu, Weidi Xie, Min Chen, and Victor Adrian Prisacariu. Nerf-: Neural radiance fields without known camera parameters. 2021. 6
- [48] Liwen Xiao, Wenze Liu, Zhicheng Wang, Yiran Wang, Zhiyu Pan, Hao Lu, and Zhiguo Cao. Densely activated self-attention for semantic segmentation. *Pattern Recognition*, page 111920, 2025. 1
- [49] Jiabo Xu, Hengming Dai, Xiangyun Hu, Shichao Fan, and Tao Ke. Scream: Scene rendering adversarial model for low-and-non overlap point cloud registration. *IEEE Transactions on Geoscience and Remote Sensing*, 2024. 5
- [50] Weiyi Xue, Zehan Zheng, Fan Lu, Haiyun Wei, Guang Chen, et al. GeoNLF: Geometry guided Pose-Free Neural LiDAR Fields. *Advances in Neural Information Processing Systems*, 37:73672–73692, 2024. 1, 2, 3, 4, 5, 6, 7, 8

- [51] Ze Yang, Yun Chen, Jingkang Wang, Sivabalan Manivasagam, Wei-Chiu Ma, Anqi Joyce Yang, and Raquel Urtasun. Unisim: A neural closed-loop sensor simulator. In *Proceedings of the IEEE/CVF Conference on Computer Vision and Pattern Recognition*, pages 1389–1399, 2023. [1](#)
- [52] Shangshu Yu, Xiaotian Sun, Wen Li, Qingshan Xu, Zhimin Yuan, Sijie Wang, Rui She, and Cheng Wang. STGC-NeRF: Spatial-Temporal Geometric Consistency for LiDAR Neural Radiance Fields in Dynamic Scenes. In *Proceedings of the AAAI Conference on Artificial Intelligence*, pages 9644–9652, 2025. [1](#), [2](#), [3](#), [6](#)
- [53] Junge Zhang, Feihu Zhang, Shaochen Kuang, and Li Zhang. Nerf-lidar: Generating realistic lidar point clouds with neural radiance fields. In *Proceedings of the AAAI Conference on Artificial Intelligence*, pages 7178–7186, 2024. [1](#), [2](#)
- [54] Richard Zhang, Phillip Isola, Alexei A Efros, Eli Shechtman, and Oliver Wang. The unreasonable effectiveness of deep features as a perceptual metric. In *Proceedings of the IEEE Conference on Computer Vision and Pattern Recognition*, pages 586–595, 2018. [6](#)
- [55] Zehan Zheng, Fan Lu, Weiyi Xue, Guang Chen, and Changjun Jiang. Lidar4d: Dynamic neural fields for novel space-time view lidar synthesis. In *Proceedings of the IEEE/CVF Conference on Computer Vision and Pattern Recognition*, pages 5145–5154, 2024. [1](#), [2](#), [3](#), [5](#), [6](#), [7](#)